Ocean Engineering 246 (2022) 110621

Contents lists available at ScienceDirect

Ocean Engineering

journal homepage: www.elsevier.com/locate/oceaneng

Numerical study of shallow-draft air-cavity hull with two-step bottom in deep and shallow water

Konstantin I. Matveev

School of Mechanical and Materials Engineering, Washington State University, Pullman, WA, 99164, USA

ARTICLE INFO

Keywords:
Air-cavity boat
Stepped hull
Shallow water
Computational fluid dynamics

ABSTRACT

Air-cavity boats utilize air injection to the bottom hull surface to reduce water drag. While being attractive due to potentially large energy savings, this technology has not yet found broad applications due to challenges in confidently predicting air-cavity flows and a lack of standard development practices for air-cavity vessels. In this work, computational fluid dynamics modeling is undertaken to demonstrate the air-cavity system implementation on a simple shallow-draft hull. After conducting verification and validation study with data available for a displacement barge-type air-cavity boat, its hull is numerically modified with intention to operate at higher speeds up to the planing regime. The modifications include replacement of a sloping beach in the bottom recess with additional step and reduction of skeg volume. Computational simulations are carried out for the modified hull at several speeds and center of gravity positions. Numerically obtained resistance, trim, heave, and air-cavity shapes are reported and discussed. A favorable loading condition is identified. In addition, simulations were conducted for shallow-water scenarios. In steady-state regimes, significant performance degradation is found near the critical speed, while performance gains are demonstrated in the supercritical regime. In one case of extremely shallow water, the hull exhibited vertical-plane instability resulting in cyclic motions.

1. Introduction

Drag reduction of ships is an important contemporary goal of marine engineering. Decrease of resistance can lead to fuel savings, reduction of pollutant emissions, and increase of speeds of marine transports. One of the promising approaches involves air supply to the hull bottom with the purpose to separate a substantial fraction of the underwater hull surface from contact with water, thus reducing its frictional drag. This technique has been under investigation for more than a century (Latorre, 1997) and prototype boats using different air-lubrication systems have started to appear (Matveev, 1999; Pavlov et al., 2020).

A schematic example of two possible air-cavity hulls is shown in Fig. 1, while several other configurations exist. The lower speed setup (Fig. 1a) allows for several waves to be present in the bottom recess with eventual reattachment of the water surface to the sloping “beach” at the rear end of the recess. At higher speeds, the length of waves on the air-water interface (cavity boundary) quickly increases, as it scales with the velocity squared (Matveev, 1999). The wavelength and wave height can become bigger than the hull length and allowable recess height, respectively. In that case, in order to ensure relatively smooth reattachment of air cavities to the hull, a horizontal (or close to horizontal) solid surface needs to be placed on the bottom behind the step to accommodate a cavity with length significantly shorter than the wavelength. Using a step of large height would reduce the useable hull volume and also lead to a big drag penalty when the air cavity is not present. Thus, a series of smaller steps with separate air cavities is better suited for semi-displacement and semi-planing hulls (Fig. 1b). It should be noted that for even faster planing hulls, a single step with a small height is usually sufficient, since the water rise behind the step is relatively minor over a distance comparable with the hull length.

Despite attractiveness of the air-cavity drag reduction method, broad implementation of this technology has not yet materialized. Some of the difficulties include a lack of understanding of how to efficiently design air-cavity hulls and how to maintain their high hydrodynamic performance in a broad range of operational and environmental conditions. The physics of relevant multi-phase flows in the proximity to solid hull surfaces and in the presence of gravity is rather complex (Arndt et al., 2009; Ceccio, 2010). In the past, simplified models based on the potential flow theory have been used to approximately predict air cavity shapes under hulls (Butuzov, 1988; Matveev, 2012). Nowadays, with growing availability of computational resources, one can expect that numerical hydrodynamics tools can be used for predicting this flow type

---

E-mail address: matveev@wsu.edu.

https://doi.org/10.1016/j.oceaneng.2022.110621
Received 19 September 2021; Received in revised form 28 November 2021; Accepted 14 January 2022

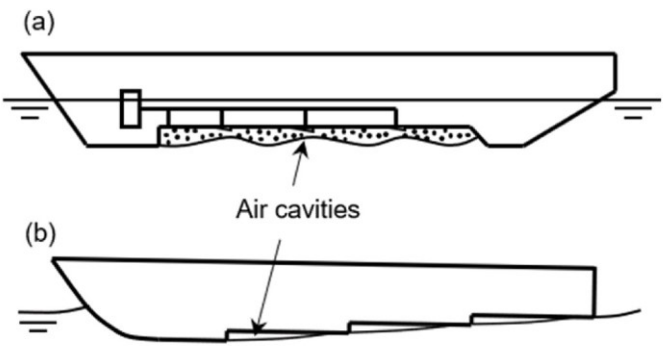

Fig. 1. Schematic of air-cavity hulls intended for (a) low-speed displacement regime and (b) fast semi-planing regime.

more reliably, thus assisting naval architects in the air-cavity ship development.

Several computational fluid dynamics (CFD) simulations investigations on air-lubricated hulls have been recently reported. Among these studies, Shiri et al. (2012) attempted modeling of the air-cavity setup tested in a cavitation tunnel. They documented significant sensitivities of the air-cavity wave properties to the air pressure in the cavity and water speed. Cucinotta et al. (2018) investigated a more or less conventional hard-chine planing hull retrofitted to accommodate an air-cavity system. They evaluated application of CFD by comparing numerical and test results and found generally acceptable agreement. Hao et al. (2019) reported a study on a model-scale displacement vessel with a recessed bottom and air injection and determined that the resulting propulsive power savings could reach 15%. Matveev and Collins (2021) validated a CFD simulation of high-Reynolds-number air-cavity flow and investigated how a morphing hull can be used to broaden the favorable speed range when a stable long cavity is present. It should be noted that numerical modeling challenges of air-cavity flows still exist, especially in the cavity reattachment regions with highly disturbed flow (e.g., Mukha and Bensow, 2020). There was also an investigation relevant to this work where an air cavity under a flat plate manifested length increases with decreasing water depths (Zverkhovskyi, 2014).

Most previously reported studies of air-cavity systems focused on either slow displacement vessels or traditional fast hulls intended for planing regimes or experimental recessed/stepped-plate setups. The main contribution of the present work is the hydrodynamic analysis of a special landing-class air-cavity hull with less conventional but relatively simple shape moving at fast but pre-planing speeds. In addition, shallow-water effects on the air-cavity hull performance have been investigated and reported, which also represent an addition to the literature on the air-cavity technology.

In this work, the state-of-the-art CFD software Star-CCM+ has been applied to model hydrodynamics of a wide-beam, shallow-draft air-cavity hull. Test data previously obtained for a displacement-type hull (similar to that shown in Fig. 1a) in a relatively fast regime are used here for verification and validation study, while employing numerically economical grids. This shallow-draft experimental hull resembles a barge but with more sophisticated bow shape. The main goal of this work is to computationally model and investigate hydrodynamic performance of a hull modified for high-speed operations in the semi-planing mode, when hydrodynamic forces provide significant lift to the hull. Thus, the hull geometry was adjusted in the numerical software to create a setup similar to that in Fig. 1b, which is more appropriate for fast regimes. After that, parametric simulations have been carried out for several speeds and center-of-gravity locations, and then in shallow-water conditions. For finite-depth effects on hull hydrodynamics of relevance to the current work, one can refer to previous studies of planing hulls (Toro, 1969; Morabito, 2013; Matveev, 2018). The present numerical results provide insights on air-cavity systems that can be helpful for developers of advanced air-assisted marine craft.

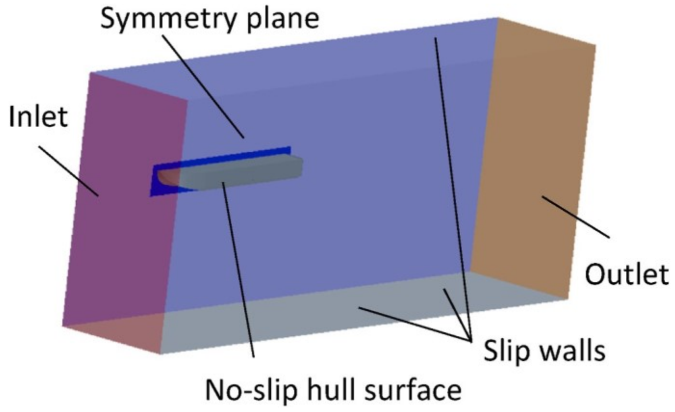

Fig. 2. Computational domain and boundary conditions.

2. Numerical approach

Computational simulations of flow around air-cavity hulls, as well as 2-DOF (heave and pitch) motions of a rigid-body hull in response to fluid and gravity forces, has been accomplished in this work using CFD software Star-CCM+ (2021). It employs a finite-volume segregated viscous solver for the fluid flow. The second-order discretization in space and the first-order in time were utilized (Ferziger and Peric, 1999). Water was considered as a constant-density fluid, and air was modeled as an ideal gas. The Eulerian multiphase approach based on the volume-of-fluid (VOF) method (Hirt and Nichols, 1981) was employed. Gravity and surface tension were also included.

The Reynolds-averaged Navier-Stokes equations (RANSE) used in the present simulations involve the continuity and momentum governing equations,

$$\frac{\partial \rho}{\partial t}+\frac{\partial\left(\rho u_j\right)}{\partial x_j}=0, \tag{1}$$

$$\frac{\partial(\rho u_i)}{\partial t}+\frac{\partial\left(\rho u_i u_j\right)}{\partial x_j}=-\frac{\partial p}{\partial x_i}+\frac{\partial}{\partial x_j}\left[\mu\left(\frac{\partial u_i}{\partial x_j}+\frac{\partial u_j}{\partial x_i}-\frac{2}{3}\delta_{ij}\frac{\partial u_k}{\partial x_k}\right)-\rho\overline{u_i' u_j'}\right]+\rho f_i, \tag{2}$$

where u_i is the Reynolds-averaged velocity, p is the pressure, ρ is the effective density, f is the body force, and $-\rho\overline{u_i' u_j'}$ is the Reynolds turbulent stresses. The mixture density ρ and viscosity μ are computed as $\rho = \rho_a\beta + \rho_w(1-\beta)$ and $\mu = \mu_a\beta + \mu_w(1-\beta)$, where β is the volume fraction of air, and indices a and w designate air and water, respectively. The Boussinesq hypothesis gives the expression for the Reynolds stresses,

$$-\rho\overline{u_i' u_j'}=\mu_t\left(\frac{\partial u_i}{\partial x_j}+\frac{\partial u_j}{\partial x_i}-\frac{2}{3}\delta_{ij}\frac{\partial u_k}{\partial x_k}\right)-\frac{2}{3}\rho k\delta_{ij}, \tag{3}$$

where μ_t is the turbulent viscosity and k is the turbulent kinetic energy. To model turbulent stresses, the realizable $k-\varepsilon$ model was applied (Rodi, 1991), which the most commonly used turbulent model in ship hydrodynamics (De Luca et al., 2016). Another popular approach, the $k-\omega$ model, was also tried in this study, producing similar results.

The turbulent kinetic energy k, the turbulent dissipation rate ε, and the turbulent viscosity μ_t are governed in the realizable $k-\varepsilon$ model by the following equations,

$$\frac{\partial(\rho k)}{\partial t}+\frac{\partial\left(\rho k u_j\right)}{\partial x_j}=\frac{\partial}{\partial x_j}\left[\left(\mu+\frac{\mu_t}{\sigma_k}\right)\frac{\partial k}{\partial x_j}\right]+G_k-\rho\varepsilon, \tag{4}$$

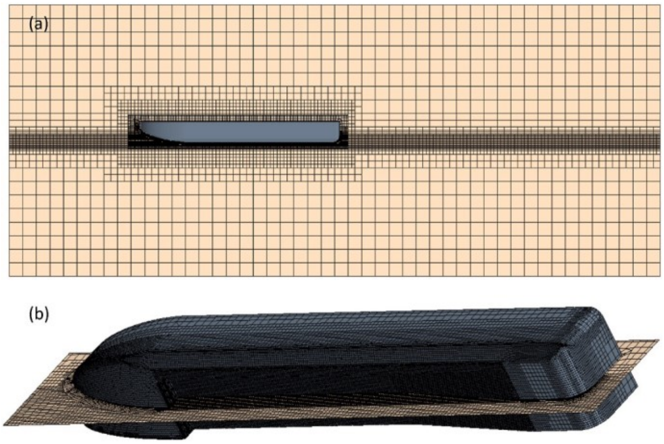

Fig. 3. Numerical mech: (a) in vertical-plane section along flow, (b) on half-hull surface and in longitudinal plane of overset region.

$$\frac{\partial(\rho\varepsilon)}{\partial t}+\frac{\partial(\rho\varepsilon u_j)}{\partial x_j}=\frac{\partial}{\partial x_j}\left[\left(\mu+\frac{\mu_t}{\sigma_\varepsilon}\right)\frac{\partial\varepsilon}{\partial x_j}\right]+\rho C_{\varepsilon1}S\varepsilon-\rho C_{\varepsilon2}\frac{\varepsilon^2}{k+\sqrt{\nu\varepsilon}}, \qquad (5)$$

$$\mu_t=\rho C_\mu\frac{k^2}{\varepsilon}, \qquad (6)$$

where G_k is the turbulent production term, S is the modulus of the mean strain rate, ν is the kinematic viscosity, and σ_k, σ_ε, $C_{\varepsilon1}$, $C_{\varepsilon2}$, C_μ are the model coefficients (Star-CCM + Manual, 2021).

The numerical domain is created to model only half of the flow (on the port side) assuming symmetry with respect to the hull centerplane (Fig. 2). The domain length, height and width are selected as 12, 5, and 2.5 of the hull beams. The no-slip wall condition is imposed on the hull surface, whereas the top and bottom boundaries of the domain are treated as slip walls. The velocity inlet and the pressure outlet are assigned at the upstream and downstream boundaries, respectively. A small air inlet is placed on the recess ceiling near the step, which is handled as an inlet with velocity matching given air supply rates. In additional shallow-water simulations reported in the Results section, the bottom boundary of the domain was shifted upward to provide a desired water depth, while the boundary condition on that surface was changed to the velocity inlet with horizontal velocity ensuring that water on the seabed was moving at a constant speed with respect to the horizontal hull position.

Numerical grids in this study were generated using the overset methodology. The non-moving background mesh spanning the entire numerical domain consists of hexahedral cells with refinement regions around the free surface and around the hull (Fig. 3a). The overset mesh was constructed near the hull; and it was able to move together with the hull in simulations. This grid had even finer cells in the hull recess in order to accurately capture the air-water interface of the bottom cavity. One of the goals in the present computational study was to keep the numerical mesh economical with the overall cell counts under one million. The numerical cell thicknesses at the wall were primarily about 30–80 of Y_+ values, which implies utilization of the wall function methodology to model boundary layers.

The time step in simulations was selected below the value given by 0.01L/U, where U is the incident flow velocity and L is the hull length, in accordance with ITTC recommendations (2014). While the simulations were unsteady, only steady-state results are reported here that corresponded to times (usually about 10–20 s from the start of simulation) when time-averaged flow characteristics no longer evolved.

3. Verification and validation study

Although many papers on testing of air-cavity hulls have been published, exact geometrical models of fast landing-class hulls with large block coefficient of interest in this study are not readily available. Thus, for the verification and validation (V&V) example of the employed numerical approach, a model-scale barge-type air-cavity hull was chosen (Fig. 4), for which test data were obtained at relatively high Froude numbers (Matveev et al., 2015). The present numerical approach has been also previously validated for a larger number of variables (drag, trim, cavity length and pressure) over broader range of experimental conditions obtained with the upgraded version of this boat. Detailed results have been presented by Collins et al. (2021). Good prediction was demonstrated for trends in all measured characteristics, and a reasonable quantitative agreement between numerical and test data was established.

The physically tested air-cavity platform was a barge-type hull with a ski-type bow, which allowed this self-propelled boat to achieve relatively high speeds. The boat has a shallow draft and a wide beam, so one of potential applications of such a hull can be for shallow-water and landing operations. This model-scale hull of length 1.51 m and beam 0.40 m has a bottom recess with a sloping “beach,” as illustrated in Fig. 5a. The experimental condition chosen for the current V&V corresponded to mass 16.8 kg, speed 1.47 m/s, air supply rate 55 sccs, and small bow-up trim of 0.2°. The hull speed can be expressed via non-dimensional Froude numbers often used in fast boat hydrodynamics,

Fig. 4. Experimental air-cavity hull on water and view of its bottom recess.

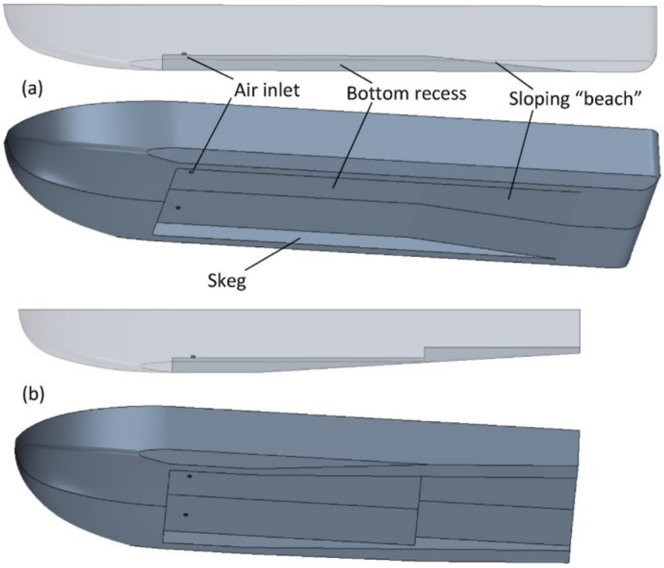

Fig. 5. Semi-transparent side views and isometric views of (a) original displacement hull and (b) modified semi-planing hull.

Table 1
Steady-state drag values on different grids for tested hull.

Mesh	Cell count	Drag
Coarse	33066	12.57 N
Medium	107367	10.92 N
Fine	668596	11.28 N

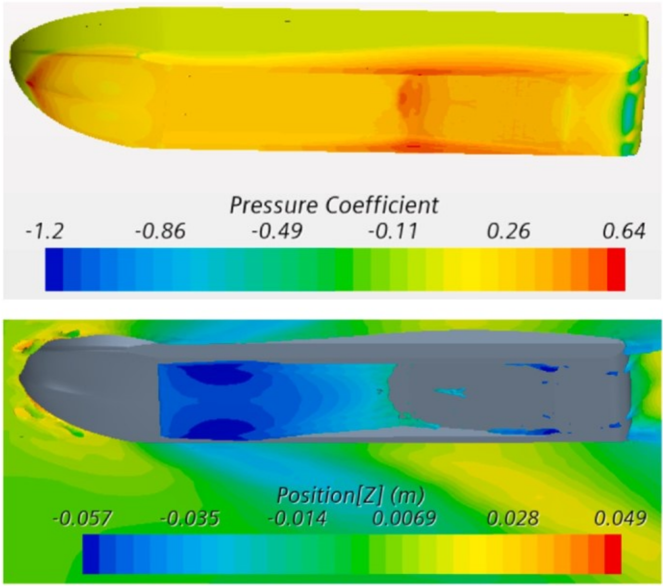

Fig. 6. Bottom views on pressure coefficient and water surface elevations on fast displacement hull.

$$Fr_{Lw} = \frac{U}{\sqrt{g L_w}}, \tag{7}$$

$$Fr_V = \frac{U}{\sqrt{g \sqrt[3]{V}}} \tag{8}$$

where L_w is the static waterline length, V is the volumetric displacement, and g is the gravitational constant. For the selected experimental condition, the Froude numbers are $Fr_{Lw} = 0.44$ and $Fr_V = 0.93$, which indicate the fast displacement mode, but far from the planing regime that usually starts near or above $Fr_{Lw} \sim 1$ and $Fr_V \sim 2.5$.

For the mesh-dependency study, three numerical grids of different mesh density (coarse, medium, fine) were generated with the ratio of 2 between numerical cell's linear dimensions. The overall cell count in the fine mesh was about 700 K. The simulations were run on these grids at the test condition. The results for the drag values obtained in steady states (given in Table 1) demonstrate oscillatory convergence with respect to the mesh density.

To estimate numerical uncertainty for the drag force, the standard method has been employed (Xing and Stern, 2010). First, the Richardson extrapolation was applied to evaluate an expected correction δ_{RE} to the solution on the fine mesh (Ferziger and Peric, 1999),

$$\delta_{RE} = \frac{\Delta_{12}}{\beta^p - 1}, \tag{9}$$

$$p = \frac{\log(\Delta_{23}/\Delta_{12})}{\log(\beta)}, \tag{10}$$

where Δ_{12} is the difference of solutions found on the fine and medium grids, Δ_{23} is the difference of solutions on the medium and coarse grids, β is the ratio of grid refinement, and p is the observed order of accuracy. Then, δ_{RE} was multiplied by a safety factor (Xing and Stern, 2010) to estimate the numerical uncertainty, which in this case was found to be 0.32 N. The test value for the hull resistance was 10.69 N, whereas the experimental uncertainty was 1.05 N. Thus, the difference between numerical (Table 1) and test results is 0.59 N, while the validation uncertainty (based on a combination of experimental and numerical uncertainties) is 1.10 N. Hence, the present numerical approach has been validated for the analyzed air-cavity hull test. In this relatively fast but still displacement regime, the flow around hull is more complicated than at low speeds, so the agreement within 6% is considered satisfactory.

Illustrations of some flow features for the numerically simulated validation case are given in Fig. 6. Increased pressure on the hull surface (Fig. 6a) is visible at the water impingement zones on the bow, at the front part of the "beach" and on the side skegs. Decreased pressure is noticeable on the curved stern portion of the hull. The air cavity covers only a part of the recess ceiling (Fig. 6b) leaving almost the entire beach surface exposed to water flow. Thus, it can be argued that this displacement-type recess arrangement is not very suitable for high-speed air-cavity applications, since air is retained only on a relatively small fraction of the hull surface area, while the wetted "beach"

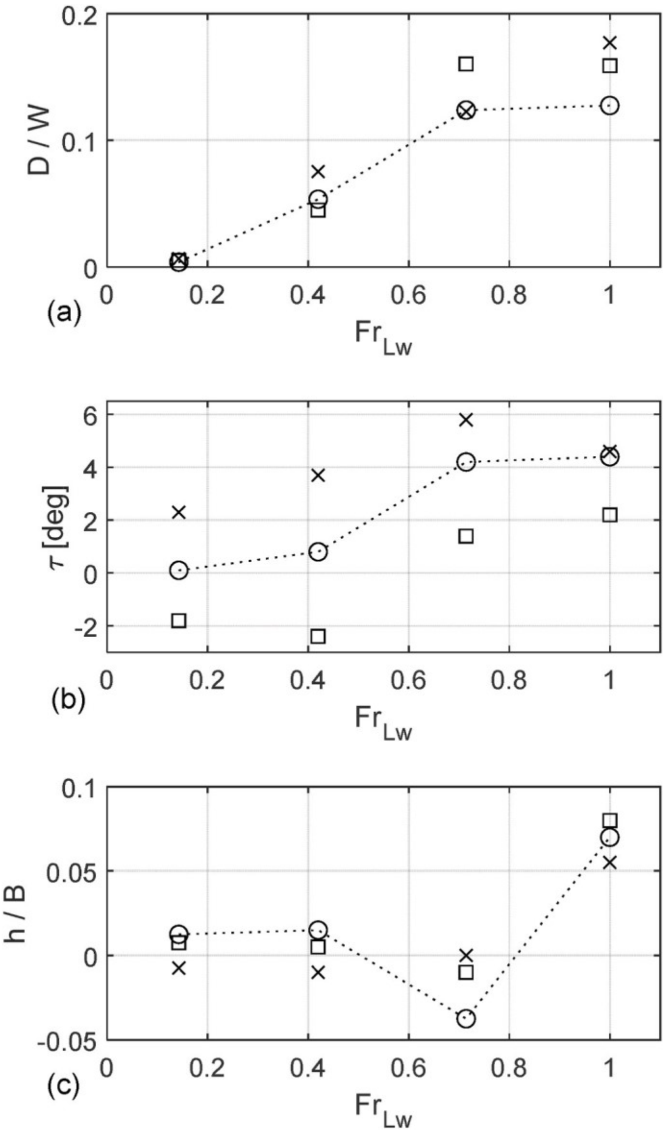

Fig. 7. (a) Drag-to-weight ratio, (b) trim, and (c) normalized heave obtained numerically for the modified hull in deep water. The center of gravity positions forward from transom: squares, $L_{cg}/B = 1.675$; circles, 1.425; crosses, 1.175. Dotted line connects data points for hull with $L_{cg}/B = 1.425$.

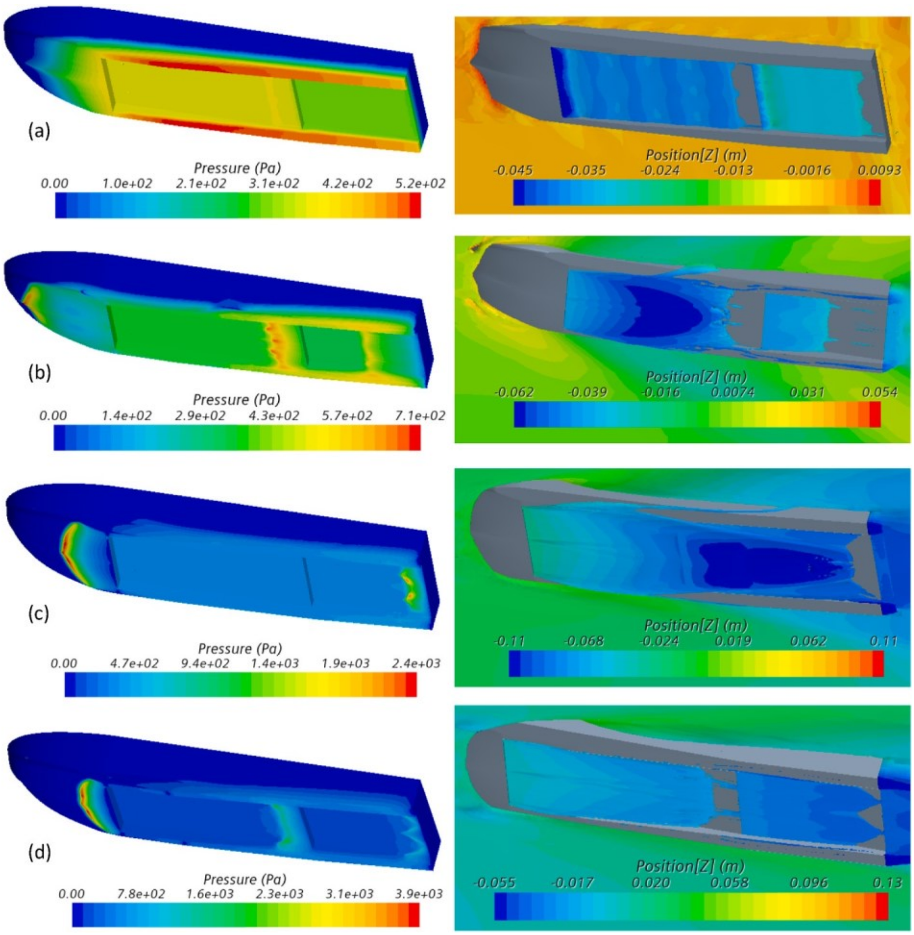

Fig. 8. Pressure distributions on hull surface and underwater views on air cavities for hull with $L_{cg}/B = 1.425$. Length-based Froude numbers Fr_{Lw}: (a) 0.14, (b) 0.42, (c) 0.71, (d) 1.00.

contributes to both pressure and friction drag.

4. Parametric results for two-step hull

In order to make the previously tested hull more suitable for higher speeds up to the planing mode, the hull geometry is modified by (i) replacing the “beach” section of the recess with an additional step, (ii) removing the stern section behind the “beach” completely while forming vertical transom, and (iii) cutting the side skegs in the inclined manner in the rear half of the hull to reduce their surface area and volume. These modifications are performed numerically in the CFD software, and the resulting hull geometry is shown in Fig. 5b.

Hydrodynamic performance of this hull was then assessed at four different speeds (from displacement to planing) to obtain drag curves. Also, three longitudinal positions of the center of gravity were tried to determine more or less optimal weight distribution, while keeping the boat mass the same as in the V&V study (16.8 kg). The studied speeds were selected as 0.5, 1.47, 2.5, and 3.5 m/s, which corresponded to Froude numbers (based on the static waterline length) $Fr_{Lw} =$ 0.14, 0.42, 0.71, 1.00 and volumetric Froude numbers $Fr_{\nabla} =$ 0.32, 0.93, 1.58, 2.21. The speed 1.47 m/s was chosen to compare the new and original hulls in the fast displacement mode, while the highest speed corresponded to the semi-planing regime. The centers of gravity were selected as 0.67, 0.57, and 0.47 m forward from the transom. Normalized to the hull beam (0.4 m), these values corresponded to $L_{cg}/B = 1.675, 1.425, 1.175$.

Larger air supply rates are generally required at higher hull speeds. Here, the flow rate of air injected into the recess air was chosen to keep the normalized air flow rate C_Q fixed, defined as follows,

$$C_Q = \frac{Q}{U h_r B_r}, \tag{11}$$

where Q is the dimensional air supply rate, U is the hull speed, and h_r and B_r are the recess height and beam, which are equal to 0.035 m and 0.3 m for the studied hull. The value for C_Q was selected as 0.02, a typical number for such air-cavity setups. The power required to pump this amount of air under the hull was below 1% of the propulsive power at higher speeds.

CFD simulations were run for these 12 cases (four speeds and three L_{cg}) with the new hull. The hull resistance, trim and heave were determined in steady-state regimes. The trim and heave were evaluated with respect to the attitude of the boat at rest with intermediate loading $L_{cg}/B = 1.425$ and no air in the recess. The drag-to-weight ratio D/W, trim τ, and heave normalized by the hull beam h/B are plotted in Fig. 7. The drag, trim and heave variations for relative CG positions 1.675 and 1.425 exhibit behavior common for planing hulls, with a significant increase of drag in the transitional regime (Fr_{Lw} around 0.42 and up to 0.71) and a modest change when approaching the planing mode (above $Fr_{Lw} = 0.71$). The heave values for these loadings are slightly higher than at rest for displacement speeds ($Fr_{Lw} = 0.14$ and 0.42) due to pressurized air pumped under the hull. At $Fr_{Lw} = 0.71$, heave becomes negative due to bottom suction experienced in the transitional regime. As the speed increases further ($Fr_{Lw} = 1.00$), the hull moves up due to substantial rise of hydrodynamic lift in the planing mode. Resistance of the rear-loaded hull increases more linearly with speed, whereas its trim peaks at $Fr_{Lw} = 0.71$. The rear-loaded hull shows a very minor suction effect at a lower speed ($Fr_{Lw} = 0.42$), while its rise at higher speeds is relatively modest.

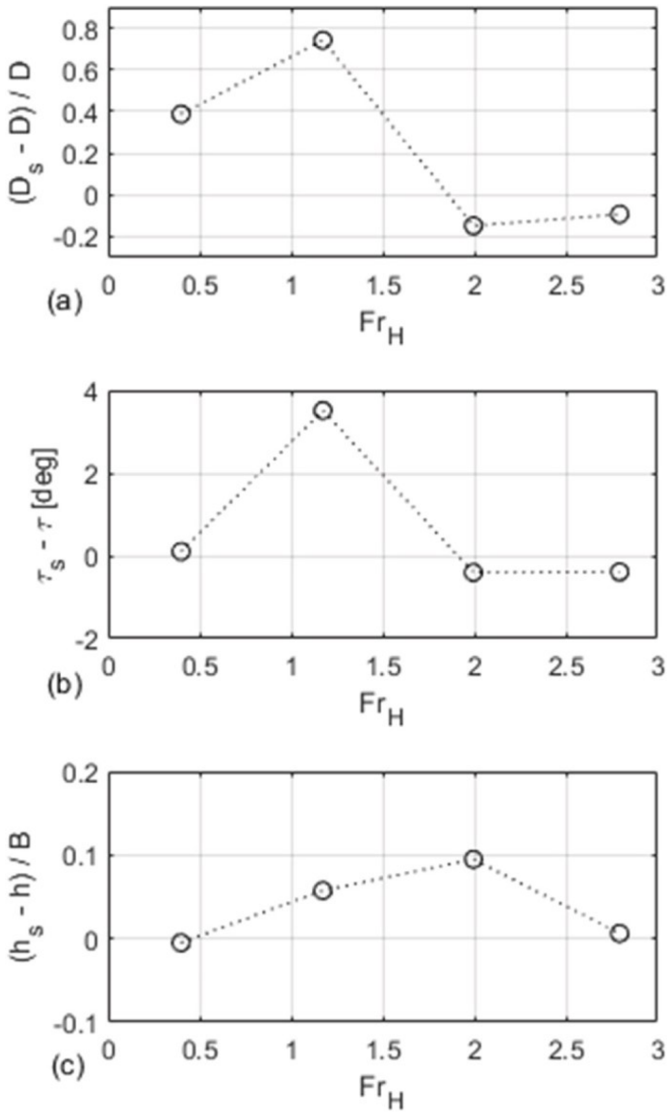

Fig. 9. Changes of (a) relative drag, (b) trim, and (c) normalized heave for the hull operating in shallow water with respect to calm-water results.

Among the studied loading distributions, the hull with $L_{cg}/B = 1.425$ manifests the best hydrodynamic performance at the highest speed (Fig. 7a). It has the lift-to-drag ratio of around 7.85, which is very good for a fast boat. At $Fr_{Lw} = 0.42$, this hull has significantly lower resistance ($D/W = 0.053$) than the original hull with a "beach" and more pronounced skegs (numerical $D/W = 0.068$), thus demonstrating benefits of implemented hull modifications even in the fast displacement mode. Also, the drag curve of the hull with $L_{cg}/B = 1.425$ is superior at most studied speeds in comparison with other loading distributions, as the front-loaded hull has substantially higher drag at $Fr_{Lw} = 0.71$ and 1.00, while the rear-loaded setup has noticeably larger resistance $Fr_{Lw} = 0.42$ and 1.00.

To provide more detailed information on air cavity shapes and pressure distributions, these characteristics are illustrated in images shown in Fig. 8 for the best-performing hull with $L_{cg}/B = 1.425$. As the hull is moving in the displacement mode at the lowest speed (Fig. 8a), the pressure distribution is nearly hydrostatic. Although the cavities ventilate the back sides of the steps, their thicknesses drop further downstream, exposing internal side walls of the skegs to the water flow. One can also notice several waves on the front cavity surface and wetted transom. In the faster but still displacement mode (Fig. 8b), elevated pressure zones on the hull surface are present at the water impingement locations: on the bow and behind both cavities. Lower pressure area is noticeable on the curved bow section in front of the first step. Pressure inside the cavities is more or less uniform. At this speed, the air escapes from the front cavity not only into the downstream cavity but also along the skegs bottoms and even laterally to the atmosphere. These mechanisms are likely caused by reduced pressure at the skeg edges. The transom becomes fully ventilated with atmospheric air at this speed.

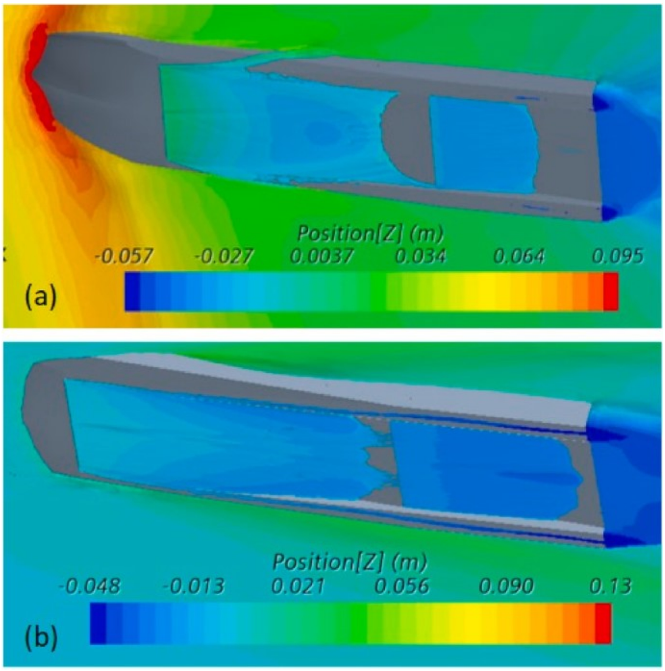

Fig. 10. Underwater views on air cavities for hull in shallow water at water-depth-based Froude numbers Fr_H: (a) 1.17, (b) 2.79.

As the speed of the hull increases (Fig. 8c), the wetted hull area decreases, since the air cavity becomes larger. A well-pronounced, wide high-pressure zone is formed on the bow, while only relatively small area near the transom manifests high pressure. A single air cavity is generated in this condition, as the front and rear cavities merge together. Again, the side-wise air leakage is noticed not far behind the front step. At the highest speed (Fig. 8d), the hull starts rising up, and its resistance is almost the same as at the lower speed (Fig. 7a). Two separate air cavities are again present on the hull bottom occupying most area in the recess, while air leaving from the front cavity enters the second cavity. Again, a high-pressure zone appears on the bow, and two areas with elevated but lower pressure are formed on the recess ceilings behind the air cavities.

One can notice that at the highest speed (Fig. 8d) the water impingement zone at the bow approaches the front step. Further speed increase may lead to the exposure of the front step to the atmosphere, which may be accompanied by more disturbed water impingement and air leakage in the forward direction. That would produce a limitation for further speed growth, if high performance (low drag and stable motion) is desired. There are also opportunities to further improve performance of this hull by trying to keep the side surfaces dry at high speeds. This can be achieved with either spray rails or more sophisticated chine design.

One of envisioned applications for the considered hull involves operations in shallow waters. To illustrate influence of finite water depths on hydrodynamics of the hull with favorable loading in the deep water, an additional set of simulations has been carried out in the numerical domain with the water depth normalized by the hull beam of $H/B = 0.4$. The differences between shallow-water and deep-water results for the drag, trim and heave are given in Fig. 9, where subscript s corresponds to shallow-water values. For the normalized speed, the water-depth Froude

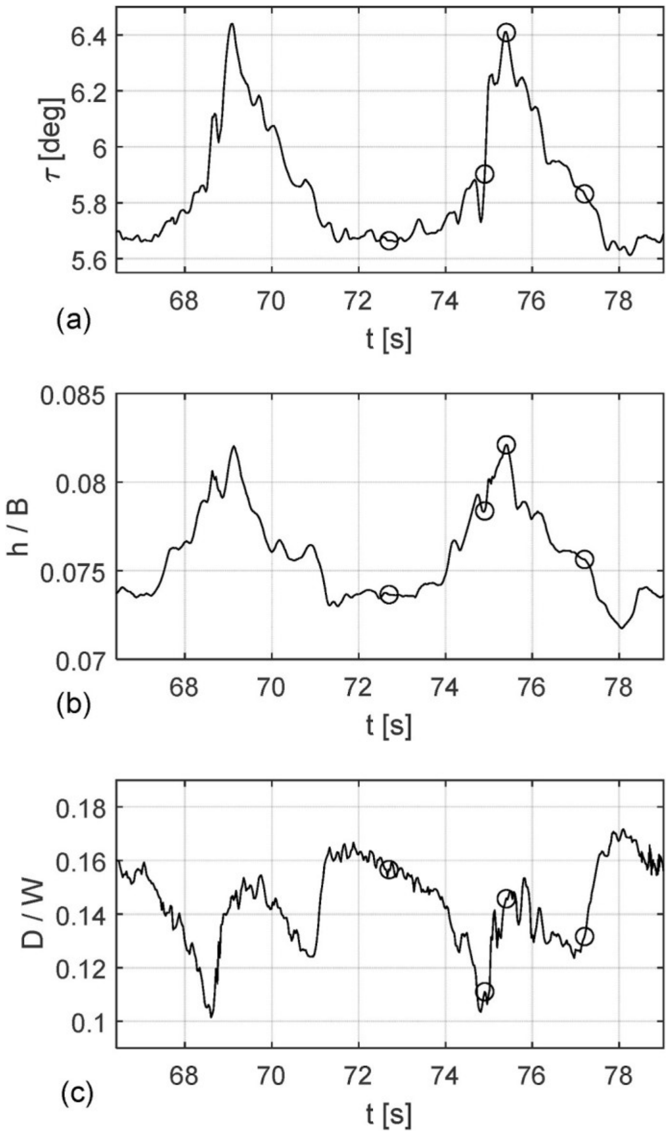

Fig. 11. Time variations of (a) trim, (b) normalized heave, and (c) drag-to-weight ratio in very shallow water at $Fr_H = 3.95$. Circles indicate time moments for which the flow field variables are presented in Fig. 12.

number is used here, $Fr_H = U/\sqrt{gH}$, as it is more appropriate for discussion of shallow-water results. The hull's absolute speeds and the waterline-length-based Froude numbers Fr_{Lw} were the same as in the previous cases in deep water.

In Fig. 9a, one can notice that the hull drag increases by 39% at the lower speed and by 74% when Fr_H is near 1. The first speed corresponds to the subcritical regime, when the hull resistance is known to moderately rise with decreasing water depth. The second speed is close to the critical regime, when a very large resistance increase can be expected due to formation of a big (the so-called "soliton") wave. It leads to substantial increases in trim and heave of the hull in this condition (Fig. 9b and c). When the boat operates at higher speeds with Fr_H noticeably greater than one (i.e., in the supercritical regime), the finite-depth effects become beneficial, as the hull trim decreases, while the hull rides higher (Fig. 9b and c). These effects result in lower drag values in comparison with the deep-water results (Fig. 9a). The boat's behavior in the finite-depth water observed in this numerical study is consistent with experimental results for conventional planing hulls in shallow water conditions (Toro, 1969; Morabito, 2013).

The air-water interfaces near the studied hull are shown for $Fr_H =$ 1.17 and 2.79 in Fig. 10. One can notice a formation of a big wave with elevated water surface in the bow region at $Fr_H = 1.17$. As the hull has a large trim angle in this case, the areas covered by air cavities become smaller (Fig. 10a). For the hull moving in the supercritical mode, the effect of the seafloor on the cavities is relatively minor, if one compares Figs. 8d and 10b. Thus, it can be recommended to avoid operating near the critical speed during longer runs in shallow waters, while one can try to take advantage of better performance at higher speeds.

One more simulation was conducted for even shallower water depth $H/B = 0.2$ at the highest speed $Fr_{Lw} = 1.00$, corresponding to $Fr_H = 3.95$. In contrast to previous cases, the air-cavity hull manifested vertical-plane instability resulting in repeatable cycles. The time histories of pitch, heave and drag-to-weight ratio in two such cycles are shown in Fig. 11. The underwater images of the air cavities under the hull and the centerplane pressure coefficient map in the fluid domain are given in Fig. 12 for four characteristic stages in a cycle at time moments indicated by circles in Fig. 11.

At the first time 72.7 s, the hull is in the lower position with low pitch (Fig. 11a and b and 12a). The highest-pressure zone on the hull is located in front of the first step and two other regions with elevated pressure are positioned at the water impingement points behind the first and second cavities. The pressure inside the first cavity is only slightly above atmospheric, while the second cavity has negative gage pressure. This suggests that air cavities do not significantly contribute to the lift of the hull at this instant in contrast to steady-state operations in deeper water (Fig. 8). As the seabed floor partially suppresses air leakage from the cavity, the air accumulating in the hull recess builds up pressure that leads to the rise of both heave and pitch (Fig. 11a and b at 74.9 s and 12b), while the wetted bow section in front of the recess decreases. Eventually, around time 75.4 s, the hull reaches an elevation when the front step comes out of water and the front air cavity establishes contact with atmosphere (Fig. 12c). In this part of the cycle, the high-pressure zone shifts from the bow to a place behind the first cavity, where water flow impinges on the recess ceiling. The secondary zone with slightly elevated pressure is located behind the second cavity. Due to large opening to atmosphere of the first cavity, the air easily escapes, and together with the rearward shift of the water impingement zone, this results in the opposite hull motion towards lower pitch and deeper position of the hull in the water (Fig. 11a and b at 77.2 s and Fig. 12d). The pressure pattern with three elevated pressure zones gradually recovers. These cycles continue repeating with a period of about 6 s.

During these oscillations in very shallow water, the hull resistance also demonstrates significant fluctuations with minima occurring slightly prior to the moments with the highest heave and pitch (Fig. 11c), when the air cavities are larger and wetted areas are smaller (Fig. 12b). The drag-to-weight ratio averaged over a cycle comes to about 0.149, implying that the averaged resistance is now 17% higher than in deeper water. Hence, when designing air-cavity hulls that may encounter extremely shallow water while moving at high speeds, one needs to be aware of vertical-plane motion instabilities and associated drag increase.

5. Conclusions

This study has demonstrated how application of computational fluid dynamics can be used for analysis of air-cavity hull hydrodynamics. Validation was performed for one test condition of a model-scale displacement-type hull, followed by parametric simulations of a hull modified for high-speed operations. By varying a position of the gravity center, a configuration with the highest performance in deep water was found when the center of gravity was located at 42.5% of the hull length forward of transom. This hull reached the drag-to-weight ratio of 0.127 at the length Froude number of 1.0, while demonstrating good performance in the entire speed range. The illustrations of the air-cavity interfaces and pressure distributions on the hull surface provide insights on the speed-dependent evolution of the air-cavity patterns and hull

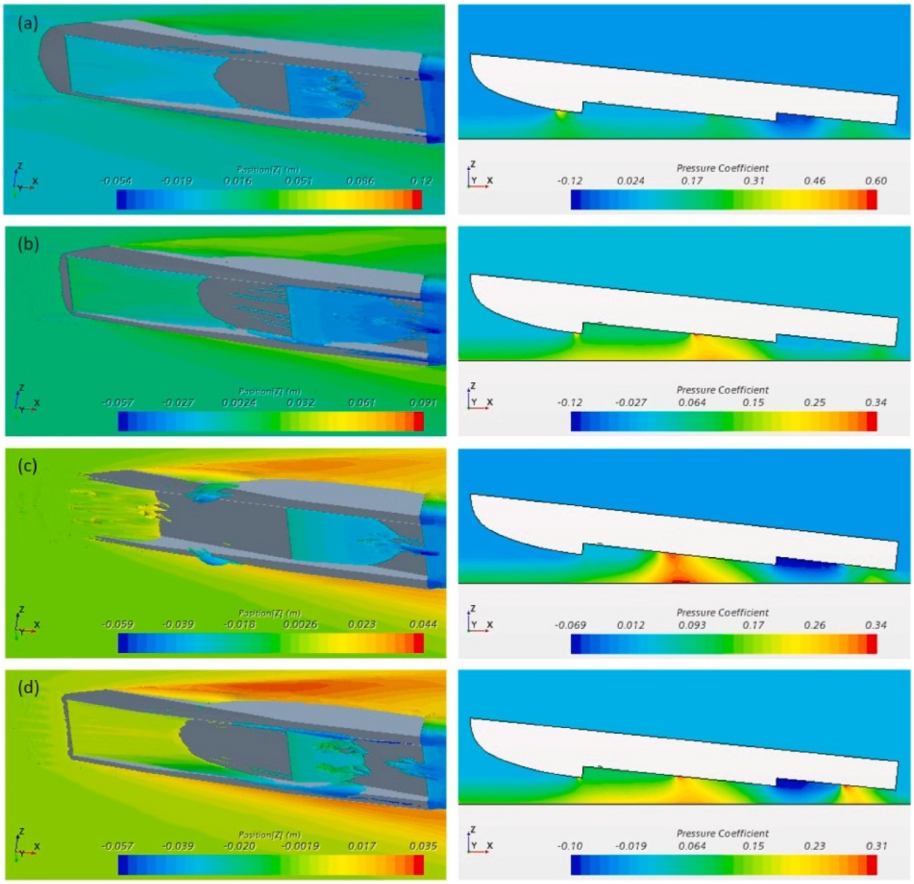

Fig. 12. Underwater views on air cavities on the bottom and pressure coefficient in the centerplane at four time moments indicated in Fig. 11 at $Fr_H = 3.95$.

loads. Results obtained for the hull with the same loading in shallow water at the depth-to-beam ratio of 0.4 manifested large drag increase (about 74%) near the critical speed, whereas resistance decreased by about 10% in the supercritical regime. However, when the water depth becomes very small, with depth-to-beam ratio of 0.2, hull motion instabilities were observed, accompanied by larger time-averaged drag.

As for future research directions on this topic, additional experimental data gathered in well-defined and well-controlled conditions with air-cavity hulls are needed to conduct more comprehensive validation studies. The air-cavity hull optimization can be carried out by considering more sophisticated hull shapes and appendages. Studies of air-cavity interactions with propulsors and performance of air-cavity hulls in waves are also of high practical interest.

CRediT authorship contribution statement

Konstantin I. Matveev: Conceptualization, Methodology, Software, Validation, Investigation, Visualization, Writing – original draft, Writing – review & editing.

Declaration of competing interest

The authors declare that they have no known competing financial interests or personal relationships that could have appeared to influence the work reported in this paper.

Acknowledgement

This material is based upon research supported by the U.S. National Science Foundation under Grant No. 1800135.

References

Arndt, R.E.A., Hambleton, W.T., Kawakami, E., Amromin, E.L., 2009. Creation and maintenance of cavities under horizontal surfaces in steady and gust flows. J. Fluid Eng. 131, 111301.

Butuzov, A.A., 1988. Spatial linearized problems on flow around ship with artificial cavitation. Shipbuild. Probl., Ser. Ship Des. 8, 1–18.

Ceccio, S.L., 2010. Friction drag reduction of external flows with bubble and gas injection. Annu. Rev. Fluid Mech. 42, 183–203.

Collins, J.M., Whitworth, P.R., Matveev, K.I., 2021. Experimental testing and numerical modeling of small-scale boat with drag-reducing air-cavity system. In: Proceedings of ASME Fluids Engineering Division Summer Conference. ASME paper FEDSM2021-62556.

Cucinotta, F., Guglielmino, E., Sfravara, F., Strasser, C., 2018. Numerical and experimental investigation of a planing air cavity ship and its layer evolution. Ocean Eng. 152, 130–144.

De Luca, F., Mancini, S., Miranda, S., Pensa, C., 2016. An extended verification and validation study of CFD simulations for planing hulls. J. Ship Res. 60 (2), 101–118.

Ferziger, J.H., Peric, M., 1999. Computational Methods for Fluid Dynamics. Springer, Berlin.

Hirt, C.W., Nichols, B.D., 1981. Volume of fluid (VOF) methods for the dynamics of free boundaries. J. Comput. Phys. 39 (1), 201–225.

International Towing Tank Conference, 2014. Practical Guidelines for Ship CFD Applications. Publication 7.5-03-02-03.

Latorre, R., 1997. Ship hull drag reduction using bottom air injection. Ocean Eng. 24, 161–175.

STAR-CCM+ Manual, 2021. https://www.plm.automation.siemens.com/global/en/products/simcenter/STAR-CCM.html.

Matveev, K.I., 1999. Modeling of vertical plane motion of an air cavity ship in waves. In: Proceedings of the 5th International Conference on Fast Sea Transportation, Seattle, USA.

Matveev, K.I., 2012. Transom effect on properties of air cavity under flat-bottom hull. Ships Offshore Struct. 7 (2), 143–149.

Matveev, K.I., 2018. On application of three-dimensional linearized potential-flow model for shallow-water planing. J. Ocean Eng. Sci. 3 (3), 218–222.

Matveev, K.I., Collins, J.M., 2021. Numerical investigation of high-Reynolds-number air-ventilated water flow under solid body with surface geometry variations. Fluids 6 (5), 174.

Matveev, K.I., Perry, N., Mattson, A., Chaney, C., 2015. Development of a remotely controlled testing boat platform with air-ventilated hull. J. Mar. Sci. Appl. 14 (1), 25–29.

Morabito, M.G., 2013. Planing in shallow water at critical speed. J. Ship Res. 57 (2), 98–111.

Mukha, T., Bensow, R.E., 2020. Flow dynamics in the closure region of an internal ship air cavity. Ocean Eng. 216, 108192.

Pavlov, G.A., Yun, L., Bliault, A., He, S.-L., 2020. Air Lubricated and Air Cavity Ships: Development, Design and Application. Springer, New York.

Rodi, W., 1991. Experience with two-layer models combining the k-ϵ model with a one-equation model near the wall. In: Proceedings of the 29th Aerospace Sciences Meeting, Reno, NV, USA. AIAA paper 91-0216.

Shiri, A., Leer-Andersen, M., Bensow, R.E., Norbby, J., 2012. Hydrodynamics of a displacement air cavity ship. In: *Proceedings of the* 29th Symposium on Naval Hydrodynamics, Gothenburg, Sweden.

Toro, A.I., 1969. Shallow-water performance of a planing boat. In: Proceedings of the Annual Meeting of Southeast Section of SNAME, Miami, FL.

Xing, T., Stern, F., 2010. Factors of safety for Richardson extrapolation. ASME J. Fluids Eng. 132 (6), 061403.

Zverkhovskyi, O., 2014. Ship Drag Reduction by Air Cavities. PhD thesis. Delft University of Technology, Delft, The Netherlands.